JOURNAL OF GUIDANCE, CONTROL, AND DYNAMICS
Vol. 17, No. 3, May–June 1994

Outboard Body Effects on Flexible Branch Body Dynamics in Articulated Multibody Systems

Sivakumar S. K. Tadikonda* and Harry W. Schubele†
Dynacs Engineering Co., Inc., Palm Harbor, Florida 34684

Investigations addressing modeling of component flexible bodies in articulated multibody systems have typically been concerned only with the boundary conditions at the inboard end of a body. It is shown here that the boundary conditions at the end (or joint) leading to the outboard bodies of a branch body play an important role as well, especially in nonplanar multibody systems. An example for such a system is a uniform flexible beam fixed at one end and with a rotating end mass attached at the other. The end mass is offset from, and rotates in a plane perpendicular to, the beam axis. This results in a time-varying boundary condition on the beam bending moment. Shape functions that account for this time-varying boundary condition are presented in this paper, and using these, the associated dynamic equations are derived. The performance of these shape functions is compared to that of three "traditional" mode sets, using numerical simulations. These results demonstrate the limitation of the latter mode sets.

I. Introduction

A VARIETY of methodologies have been presented in the literature to model the dynamics of articulated, flexible multibody systems (see Refs. 1–3, for example). In these methods, the small elastic motion of each body is expressed using the assumed modes method. A question that naturally arises is what type of component modes should be used to describe body flexibility. In this context, attention has often been focused only on modeling the joint location leading to the inboard branch of a body as "pinned" or "fixed" when generating the component mode set, even when a body has bodies both inboard and outboard of it. This is apparent in the use of pinned-free and fixed-free component modes to describe the flexibility of a branch body in the development of analytical models in Refs. 1 and 2. Reference 3 does not limit the use to any particular mode set. Although the component branch body flexibility models do not contain the effects due to outboard bodies, because of the free natural boundary condition at the distal end, the synthesized branch body modal equations will contain the outboard body effects. This contribution is obtained in a manner analogous to the Rayleigh-Ritz approach, by considering the component pinned-free (or fixed-free) modes as the trial functions and the outboard body effects as those due to mass and inertia augmentations.

The presence of outboard bodies in articulated multibody systems in general gives rise to time-varying forces and torques at the joint locations leading to those outboard bodies. This is the case for the system shown in Fig. 1. This system consists of a uniform flexible beam that has one end fixed and has an end mass that is rotating about the beam axis at the other. Two sets of boundary conditions are needed to solve the boundary-value problem for the beam in Fig. 1: the geometric boundary conditions (zero displacement and slope) at the fixed end and the natural boundary conditions, associated with the force and the moment balance, at the other end. The natural boundary conditions relate the translational inertia force of the end mass to the shear force in the beam, and the rotational inertia of the end mass to the beam bending moment. For a given orientation of the end mass (thus, for a given end inertia), the resulting boundary value problem can be solved using the method of separation of variables. If the end mass is rotating, however slowly, the end inertia varies, and the associated natural boundary condition changes in a continuous fashion. As a result, the characteristic behavior of the flexible beam, as indicated by the instantaneous eigenvalues, undergoes continuous change. However, the boundary condition associated with the force balance does not change. Note that this scenario is similar to a payload reorientation.

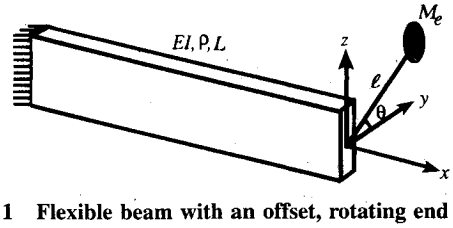

Fig. 1 Flexible beam with an offset, rotating end mass.

If the fixed end in Fig. 1 is replaced by a pinned end that permits rotation about the z axis, the resulting single flexible link manipulator can be used to position and orient a payload, within a limited workspace. Control of such a manipulator has not been pursued in the literature, to date. Although experiments involving slewing of a single flexible link have been conducted in the past (Refs. 4 and 5, for example), to the best of the authors' knowledge, none has considered a payload reorientation, similar to that shown in Fig. 1. The analytical model for a single flexible link manipulator in Ref. 6 considers and the experiment in Ref. 7 contains only a point end mass. As a first step toward understanding the issues associated with the dynamics and control of such nonplanar articulated flexible multibody systems, we investigate the effects time-varying boundary conditions have on component flexible body dynamics using the system in Fig. 1, i.e., without any articulation at the inboard end.

The objectives of this paper are threefold. The first is to demonstrate the effect of continuously-varying natural boundary conditions on component flexible body characteristic behavior, using the nonplanar system shown in Fig. 1. The second objective is to point out the difficulties that arise due to large outboard body masses and inertias if they are not accounted for when generating the component mode set. The third is the development of shape functions that account for the varying inertia end conditions. The next section addresses the first two

Received Nov. 23, 1992; revision received Sept. 20, 1993; accepted for publication Oct. 1, 1993.

*Project Engineer; currently Senior Principal Engineer, McDonnell Douglas Aerospace, Seabrook, MD 20706. Member AIAA.
†Engineering Director. Member AIAA.

objectives. The third objective is addressed in Secs. III and IV. The equations of motion obtained using the shape functions derived in Secs. III and IV are presented in Sec. V. The performance of these functions is compared with that of three traditional assumed mode sets in Sec. VI using numerical simulations. A discussion on the application to other systems is presented in Sec. VII. Finally, conclusions are presented in Sec. VIII.

II. Effect of Time-Varying Natural Boundary Conditions

Consider a uniform flexible beam fixed at one end ($x = 0$) and supporting a mass at the other ($x = L$), as shown in Fig. 1. In the coordinate system shown in Fig. 1, only the vibration of the beam in the y direction is of interest. Let ρ, EI, and L denote the mass per unit length, the stiffness, and the length of the beam, respectively. The end mass M_e is connected to the beam by a rigid massless bar of length ℓ and can rotate about the beam axis. If the inclination of the rod connecting the end mass to the beam with the y axis is denoted by θ, the end inertia and thus the boundary condition on the beam bending moment vary with θ. Consequently, as the end mass rotates about the x axis, the natural frequencies vary in a continuous fashion, although the terminology "frequency" ceases to apply. It is clear that $\theta = 0$ deg and $\theta = 90$ deg correspond to the maximum and minimum inertia end conditions for beam vibration in the y direction. The same orientations also correspond to the minimum and maximum values, respectively, for each of the beam natural frequencies.

The natural frequency variations normalized with respect to the respective minimum natural frequencies (i.e., ω_i/ω_{i0}) are shown in Fig. 2 for the first four modes. The system parameters used for this plot are: $\rho = 0.5585$ Kg/m, $EI = 46.7109$ N · m^2, $L = 1.6$ m, $M_e = 1.0$ Kg, $\ell = 1.0$ m. The ranges for the first four natural frequencies are shown in Table 1. The effect of the varying boundary condition on the system dynamics can be readily seen in both Fig. 1 and Table 1. In particular, note the 400% change in the second natural frequency. Increasing M_e (and hence I_e) tenfold results in a 900% change for the second mode. Any robust controller design for this system must then consider these large variations.

Next, we consider the dynamic modeling of the given system. Let $u(x, t)$ denote the elastic transverse displacement along the body y direction. Using the assumed modes approach,[8] we can express $u(x, t)$ as

$$u(x, t) = \sum_{i=1}^{n} \psi_i(x)\eta_i(t) \tag{1}$$

where $\psi_i(x)$ represent the assumed mode shapes, $\eta_i(t)$ are their time dependent amplitudes, and the number of retained modes is indicated by n. Note that $\psi_i(x)$ can be chosen from an admissible set.[8] Using this representation, the kinetic energy of the system can be shown to be

$$KE = \frac{1}{2}\sum_{i=1}^{n}\sum_{j=1}^{n} \times [m_{ij} + M_e\psi_i(L)\psi_j(L) + I_e\psi_i'(L)\psi_j'(L)]\,\dot{\eta}_i\dot{\eta}_j + \frac{1}{2}I_0\dot{\theta}^2 \tag{2}$$

where prime and solid dot indicate differentiation with respect to x and t, respectively,

$$m_{ij} = \int_0^L \rho\psi_i\psi_j\,dx \tag{3}$$

$$I_e = I_0\cos^2\theta \tag{4}$$

and, for the system shown in Fig. 1, $I_0 = M_e\ell^2$. The potential energy has the form

$$PE = \frac{1}{2}\sum_{i=1}^{n}\sum_{j=1}^{n} \Lambda_{ij}\eta_i\eta_j \tag{5}$$

where

$$\Lambda_{ij} = \int_0^L EI\psi_i''\psi_j''\,dx \tag{6}$$

The equations of motion can then be obtained using a Lagrangian approach as

$$\sum_{j=1}^{n} [m_{ij} + M_e\psi_i(L)\psi_j(L) + I_e\psi_i'(L)\psi_j'(L)]\,\ddot{\eta}_j - I_0\sin 2\theta\sum_{j=1}^{n}\phi_i'(L)\phi_j'(L)\eta_j\dot{\theta} + \sum_{j=1}^{n}\Lambda_{ij}\eta_j = f_i \tag{7}$$

$$i = 1, \ldots, n$$

The generalized active force for the ith mode is indicated by f_i in Eq. (7). For further reference, let M denote the system mass matrix whose elements are given by

$$M_{ij} = m_{ij} + M_e\psi_i(L)\psi_j(L) + I_e\psi_i'(L)\psi_j'(L) \tag{8}$$

The type of component modes used as well as the relative magnitudes of the end mass and end inertia will determine the behavior of the mass matrix. For example, if $\psi_i(x)$ correspond to the mass normalized fixed-free modes of a uniform flexible beam, i.e.,

$$\psi_i(x) = \frac{1}{\sqrt{\rho L}}\left\{\cos\left(\frac{\lambda_i x}{L}\right) - \cosh\left(\frac{\lambda_i x}{L}\right) + A_i\left[\sin\left(\frac{\lambda_i x}{L}\right) - \sinh\left(\frac{\lambda_i x}{L}\right)\right]\right\} \tag{9}$$

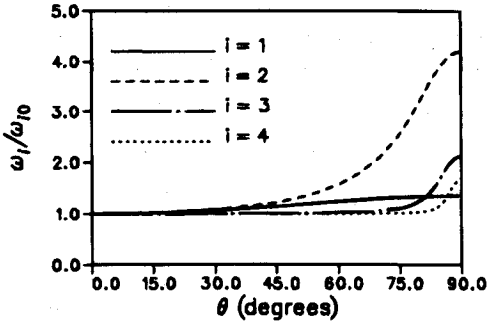

Fig. 2 Variation of frequencies with end mass orientation.

Table 1 Ranges for the first two natural frequencies

	ω_i, rad/s	
i	$\theta = 0$ deg	$\theta = 90$ deg
1	3.9352	5.3136
2	13.7741	57.7699
3	85.6874	181.4885
4	226.2647	375.4630

where $A_i = (\sin \lambda_i - \sinh \lambda_i)/(\cos \lambda_i + \cosh \lambda_i)$, and λ_i are the eigenvalues, it can be shown that

$$m_{ij} = \delta_{ij} \tag{10}$$

$$\psi_i(L) = (-1)^i 2/\sqrt{\rho L} \tag{11}$$

$$\psi_i'(L) = -\frac{2\lambda_i}{L\sqrt{\rho L}} \frac{\sin \lambda_i \cosh \lambda_i + \cos \lambda_i \sinh \lambda_i}{\cos \lambda_i + \cosh \lambda_i} \tag{12}$$

The symbol δ_{ij} denotes the Kronecker delta. For $i > 3$,

$$\frac{\sin \lambda_i \cosh \lambda_i + \cos \lambda_i \sinh \lambda_i}{\cos \lambda_i + \cosh \lambda_i} = (-1)^{i+1}$$

Thus, for $i, j > 3$,

$$M_{ij} = \delta_{ij} + (-1)^{i+j}\left(4\frac{M_e}{\rho L} + 4\lambda_i\lambda_j \frac{I_e}{\rho L^3}\right) \tag{13}$$

As the mass ratio $M_e/\rho L$, and/or the inertia ratio $I_e/\rho L^3$ increases, terms with the end mass and inertia will dominate the mass matrix. Such large mass and inertia ratios can easily lead to an ill conditioning of the mass matrix. This is especially true of the shuttle Remote Manipulator System (SRMS) or the Space Station Remote Manipulator System (SSRMS) models in which the component modal models do not contain payload effects and a 20,000-Kg payload with large rotational inertias is added as the last body in the chain.

When the eigenvalue problem associated with Eq. (7) is solved (with $\dot{\theta} = f_i = 0$) with ψ_i in Eq. (9) as trial functions, convergence will be poor. This is because the internal force and moment vanish for the cantilever modes at the free end and thus the external moment and force due to the end mass and end inertia (or outboard bodies) cannot be balanced at the free end. It was shown in Ref. 9 that violation of moment and force balance will have convergence characteristics of $\bigcirc(1/n^3)$ and $\bigcirc(1/n^4)$, respectively. Thus, n must be large to yield accurate results, especially when the moment balance cannot be achieved. However, large n also implies larger values for the elements of the mass matrix because of the associated large (component) eigenvalues.

The effects of large mass ratios can be successfully accounted for by the use of mass augmented modes. Indeed, mass augmentation alone will suffice for planar, two flexible-link manipulators such as those considered in Refs. 10 and 11, to diagonalize the associated modal mass blocks. This is because the link flexibility is assumed to be in the same plane for both the links and the joint rotational axes are perpendicular to this plane. It can be easily shown that this kinematic structure does not alter the modal mass blocks and thus component frequencies of the inboard link during any maneuver. Thus, in planar cases, if the mass augmentation is accounted for, the modal mass block will be diagonal. However, no simple solutions exist to account for the large inertias. This is because the end inertia is often a nonlinear function of the articulation angle. This effect can be substantial, as can be seen from Fig. 2, even for the case when the end mass and beam mass are of the same order. The end inertia may alter the characteristics of the system substantially, especially for nonplanar multibody systems.

The third objective of this paper, namely, to generate shape functions that account for the continuously-varying boundary conditions, is addressed next. We show that the functions thus generated also yield a diagonal modal mass block that is time invariant. The approach will be outlined using a continuum representation of the mode shapes. To this end, we propose to modify Eq. (1) as

$$u(x, \theta, t) = \sum_{i=1}^{n} \phi_i(x, \theta)\eta_i(t) \tag{14}$$

and $\phi_i(x, \theta)$ now correspond to the θ-dependent trial functions to reflect the dependency of the component dynamic behavior on the orientation of the outboard body. This is different from the traditional mode type (such as fixed free, pinned free, etc.) selection concerns where only the boundary conditions at the inboard end are considered important and the varying effects of outer bodies on component models are not considered.

The implication of Eq. (14) is that the time derivative of the elastic displacement u will now have the form

$$\dot{u}(x, \theta, t) = \sum_{i=1}^{n} \phi_i(x, \theta)\dot{\eta}_i(t) + \dot{\theta} \sum_{i=1}^{n} \frac{d}{d\theta}[\phi_i(x, \theta)]\eta_i(t) \tag{15}$$

The first term on the right side of Eq. (15) corresponds to the standard expression for elastic motion rate when time-invariant shape functions are used. The second term then represents the variation in shape functions due to changes in the orientation of the end mass.

The first step in obtaining the desired derivatives of the shape functions with respect to the end mass orientation (θ) is the generation of the shape functions as explicit functions of θ. To this end, we formulate the eigenvalue problem for a constant orientation of the end mass and obtain the eigenfunctions, in Sec. III. The derivatives of these functions with respect to the end mass orientation are obtained in Sec. IV.

III. Eigenvalue Problem for a Constant θ

For a constant orientation of the end mass, the eigenvalue problem for the vibration of the beam shown in Fig. 1 can be stated as

$$\phi''''(x) - \beta^4\phi(x) = 0, \qquad \beta^4 = \omega^2\rho/EI \tag{16}$$

with the boundary conditions

$$\phi(0) = 0, \qquad \phi'(0) = 0, \qquad EI\phi''(L) = \omega^2 I_e\phi'(L)$$
$$EI\phi'''(L) = -\omega^2 M_e\phi(L) \tag{17}$$

For the configuration shown in Fig. 1, the end inertia I_e is dependent on the orientation angle θ through Eq. (4). Thus, the eigenvalues depend on θ as well. The characteristic equation for the given system can be obtained as

$$\lambda^4 I_e(M_e/\rho L)(1 - \cos \lambda \cosh \lambda) + \rho L^3(1 + \cos \lambda \cosh \lambda)$$
$$- I_e\lambda^3(\sin \lambda \cosh \lambda + \cos \lambda \sinh \lambda)$$
$$- M_e L^2\lambda(\sin \lambda \cosh \lambda - \cos \lambda \sinh \lambda) = 0 \tag{18}$$

where $\lambda = \beta L$. The eigenfunction $\phi_r(x)$ for each solution λ_r of the characteristic equation can be shown to be

$$\phi_r(x) = A_r[\cos \beta_r x - \cosh \beta_r x$$
$$+ B_r(\sin \beta_r x - \sinh \beta_r x)] \tag{19}$$

where

$$B_r = \frac{\omega_r^2 I_e(\sin \lambda_r + \sinh \lambda_r) - EI\beta_r(\cos \lambda_r + \cosh \lambda_r)}{\omega_r^2 I_e(\cos \lambda_r - \cosh \lambda_r) + EI\beta_r(\sin \lambda_r + \sinh \lambda_r)} \tag{20}$$

$$= \frac{\omega_r^2 M_e(\cos \lambda_r - \cosh \lambda_r) + EI\beta_r^3(\sin \lambda_r - \sinh \lambda_r)}{EI\beta_r^3(\cos \lambda_r + \cosh \lambda_r) - \omega_r^2 M_e(\sin \lambda_r - \sinh \lambda_r)} \tag{21}$$

and A_r are the normalization constants satisfying

$$\int_0^L \rho\phi_r(x)\phi_s(x)\,dx + M_e\phi_r(L)\phi_s(L) + I_e\phi_r'(L)\phi_s'(L) = \delta_{rs} \quad (22)$$

and can be shown to be

$$A_r = [\rho L + \{\omega_r^2 EI\beta_r^3 I_e^2(1 - cch)(csh + sch) + (EI)^2\beta_r\rho(1 + cch)(sch - csh) + 2\omega_r^2 I_e EI\rho(sh^2 - s^2)\}/D_r]^{-1/2} \quad (23)$$

$$D_r = [\omega_r^2 I_e(c - ch) + EI\beta_r(s + sh)]^2 \quad (24)$$

A shorthand notation $s = \sin\lambda_r$, $c = \cos\lambda_r$, $sh = \sinh\lambda_r$, and $ch = \cosh\lambda_r$ is employed in the preceding equations. Equating the right-hand sides of Eqs. (20) and (21) yields the characteristic equation given in Eq. (18). In numerical simulations, it was found that the expression in Eq. (21) yielded more accurate results than the one in Eq. (20).

IV. Effect of Changing Inertia

As can be seen from Eq. (15), the derivative of the trial function $\phi_r(x, \theta)$ with respect to the orientation of the end mass is needed to compute the elastic motion rate. To this end, we differentiate Eq. (19) with respect to θ to obtain

$$\frac{d\phi_r}{d\theta} = \frac{1}{A_r}\frac{dA_r}{d\theta}\phi_r + \frac{x}{\lambda_r}\frac{d\phi_r}{dx}\frac{d\lambda_r}{d\theta} + A_r\frac{dB_r}{d\theta}(\sin\beta_r x - \sinh\beta_r x) \quad (25)$$

The closed-form expressions for $dA_r/d\theta$, $d\lambda_r/d\theta$, and $dB_r/d\theta$ are quite long. This is due to the fact that, as can be seen from Eqs. (18–24), the terms A_r, β_r, and B_r are all functions of the end mass orientation. Two of the three derivatives appearing in Eq. (25) are given next. The derivatives of the eigenvalues with respect to θ are given by

$$\frac{d\lambda_r}{d\theta} = \frac{1}{C_r}\left[\lambda_r^4\frac{M_e}{\rho L}(1 - cch) - \lambda_r^3(sch + csh)\right]\frac{dI_e}{d\theta} \quad (26)$$

where

$$C_r = [(2M_e - \rho L)L^2 + \lambda_r^4 I_e M_e/(\rho L)](s \cdot ch - c \cdot sh) - 3\rho L^3\lambda_r(1 + c \cdot ch) + I_e\lambda_r^3 M_e/(\rho L)(1 - c \cdot ch) - 2\lambda_r^3 I_e\, c \cdot ch - 2M_e L^2\lambda_r\, s \cdot sh \quad (27)$$

The notation defined earlier, following Eq. (24), is again used in the preceding equations. Differentiating Eq. (4) with respect to θ, we obtain

$$\frac{dI_e}{d\theta} = -I_0 \sin 2\theta \quad (28)$$

The variation of B_r with respect to θ is given by

$$\frac{dB_r}{d\theta} = \frac{2}{D_r}\left(G_r\frac{d\lambda_r}{d\theta} - \frac{EI\lambda_r}{L}\omega_r^2\, s \cdot sh\frac{dI_e}{d\theta}\right) \quad (29)$$

$$G_r = \omega_r^2 I_e[(\omega_r^2 I_e + 3EI/L)\, s \cdot sh - EI\beta_r(c \cdot sh + s \cdot ch) + (EI\beta_r)^2(1 + c \cdot ch)] \quad (30)$$

Thus, both $d\lambda_r/d\theta$ and $dB_r/d\theta$ vanish at $\theta = 0$ deg and $\theta = 90$-deg. The expression for $dA_r/d\theta$ is very long and hence is not given here. However, this term also vanishes for both the $\theta = 0$-deg and $\theta = 90$-deg orientations of the end mass.

V. Equations of Motion

The equations of motion are obtained using Lagrange's method. The kinetic energy of the system is formed as

$$KE = \frac{1}{2}\left[\int_0^L \rho\dot{u}^2 dx + M_e\dot{u}^2(L, t) + I_e\dot{u}'^2(L, t) + I_0\dot{\theta}^2\right] \quad (31)$$

The substitution of the modal expansion for the elastic displacement and its rate from Eqs. (14) and (15), respectively, into the kinetic energy expression just given yields

$$KE = \frac{1}{2}\sum_{i=1}^{n}\dot{\eta}_i^2 + \frac{\dot{\theta}^2}{2}\sum_{i=1}^{n}\sum_{j=1}^{n}Q_{ij}\eta_i\eta_j + \dot{\theta}\sum_{i=1}^{n}\sum_{j=1}^{n}N_{ij}\eta_i\dot{\eta}_j + \frac{1}{2}I_0\dot{\theta}^2 \quad (32)$$

where

$$Q_{ij} = \int_0^L \rho\frac{d\phi_i}{d\theta}\frac{d\phi_j}{d\theta}dx + M_e\frac{d\phi_i}{d\theta}\bigg|_{x=L}\frac{d\phi_j}{d\theta}\bigg|_{x=L} + I_e\frac{d\phi_i'}{d\theta}\bigg|_{x=L}\frac{d\phi_j'}{d\theta}\bigg|_{x=L} \quad (33)$$

$$N_{ij} = \int_0^L \rho\frac{d\phi_i}{d\theta}\phi_j dx + M_e\frac{d\phi_i}{d\theta}\bigg|_{x=L}\phi_j(L) + I_e\frac{d\phi_i'}{d\theta}\bigg|_{x=L}\phi_j'(L) \quad (34)$$

Substitution of Eq. (25) into Eqs. (33) and (34) yields long expressions for the elements of the matrices Q and N. Note that both these matrices are functions of θ.

The potential energy is simply

$$PE = \frac{1}{2}\sum_{i=1}^{n}\omega_i^2\eta_i^2 \quad (35)$$

Although the potential energy has a simple form, the ω_i are functions of the end inertia and must be calculated for every value of θ. Note that the functions $\phi_i(x, \theta)$ can no longer be called eigenfunctions because of their implicit dependency on time. Similarly, ω_i cannot be termed frequencies.

The elastic motion equations are obtained using Lagrange's equations, as

$$\ddot{\eta}_i + \ddot{\theta}\sum_{j=1}^{n}N_{ji}\eta_j + \dot{\theta}\sum_{j=1}^{n}(N_{ji} - N_{ij})\dot{\eta}_j + \dot{\theta}^2\sum_{j=1}^{n}\left(\frac{dN_{ji}}{d\theta} - Q_{ij}\right)\eta_j + \omega_i^2\eta_i = 0, \qquad i = 1 \ldots n \quad (36)$$

A comparison of Eqs. (7) and (36) reveals the absence of a payload angular acceleration term in the former model.

VI. Numerical Results

The derivatives of the eigenvalues with respect to θ, i.e., $d\lambda_i/d\theta$ ($i = 1, 2, 3$), are plotted in Figs. 3–5 for the system

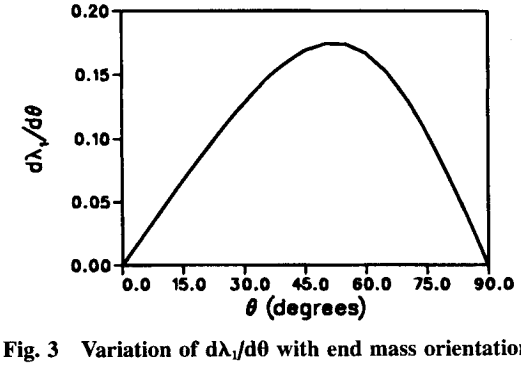

Fig. 3 Variation of $d\lambda_1/d\theta$ with end mass orientation.

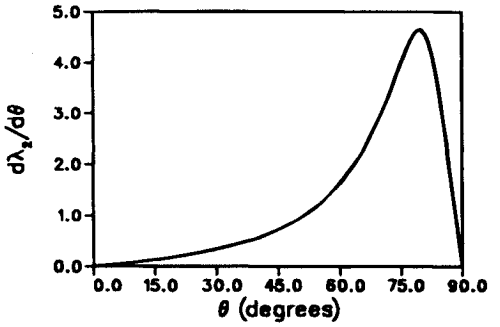

Fig. 4 Variation of $d\lambda_2/d\theta$ with end mass orientation.

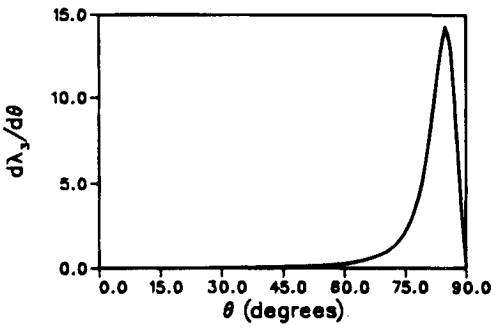

Fig. 5 Variation of $d\lambda_3/d\theta$ with end mass orientation.

parameters considered earlier. It can be seen that the changes in the values for end inertia affect the second and higher modes most. In particular, we observe from Fig. 2 that the maximum change in the natural frequency occurs for the second mode, and not the first mode. This is because, the first mode of the cantilever beam with an end mass can be closely approximated by the static deflection profile resulting from a tip force (or an end mass), where as the static deflection profile with a tip moment is required to affect the second and higher modes. The end inertia indeed provides the moment boundary condition required to affect these higher modes.

To explain the large amplitudes of $d\lambda_i/d\theta$ ($i = 2, 3$) as the end mass orientation changes, we refer to Fig. 2. We observe that significant changes in the second natural frequency occur over a range for θ of about 60 deg whereas the changes in the third and higher frequencies occur over much smaller ranges for θ. This range for θ decreases quite rapidly as the mode number increases. Thus, although the changes in ω_i ($i = 3, \ldots,$) are smaller than those in ω_2, these changes occurring over monotonously decreasing ranges for θ result in the large amplitudes shown in Figs. 4 and 5. For higher modes, the transition from a zero value to a nonzero value for the end inertia is all that matters. This is because it corresponds to the absence or presence, respectively, of a natural boundary condition in the system.

The terms N, Q, and $dN/d\theta$ are evaluated using closed-form expressions for θ between 0 deg and 90 deg in order to obtain a numerical solution to Eq. (36). From Figs. 3–5, we observe that the transition for $d\lambda_i/d\theta$ ($i = 2, \ldots,$) is rapid for θ between 70 and 90 deg. This is true for the terms N, Q, and $dN/d\theta$ as well. The analytical evaluations are performed in 5-deg steps between 0 and 70 deg and in 1-deg steps between 70 and 90 deg to accommodate the rapid changes. For other values of θ these values are linearly interpolated.

The response of the beam to an initial tip displacement, with $\theta = 45$ deg at $t = 0$ and a steady angular speed of $\dot{\theta} = 0.5$ rad/s for the end mass, is simulated next. The initial values for the modal amplitudes, for a given tip displacement, are obtained using the modal expansion in Eq. (14) as follows. Let $v(x)$ define the deflection profile at time $t = 0$. That is, $u(x, \theta, 0) = v(x)$. Then, from Eq. (14),

$$v(x) = \sum_{j=1}^{n} \phi_j(x, \theta)\eta_j(0) \tag{37}$$

Multiplying both sides by $\rho\phi_i(x, \theta)$ and integrating over the beam length we obtain

$$\int_0^L \rho v(x)\phi_i(x, \theta)\, dx = \sum_{j=1}^{n} \int_0^L \rho\phi_i(x, \theta)\phi_j(x, \theta)\, dx\eta_j(0) \qquad i = 1, \ldots, n \tag{38}$$

Thus, we obtain the following n algebraic equations for the n unknowns $\eta_j(0)$, $j = 1, 2, \ldots, n$:

$$\sum_{j=1}^{n} C_{ij}\eta_j(0) = D_i, \qquad i = 1, \ldots, n \tag{39}$$

where

$$C_{ij} = \int_0^L \rho\phi_i(x, \theta)\phi_j(x, \theta)\, dx \tag{40}$$

$$D_i = \int_0^L \rho v(x)\phi_i(x, \theta)\, dx \tag{41}$$

The integration in Eq. (40) can be avoided by using Eq. (22). Equation (39) can be written in matrix form as

$$[C]\{\eta(0)\} = \{D\} \tag{42}$$

where $\{\eta(0)\} = [\eta_1(0), \ldots, \eta_n(0)]^T$ and $\{D\} = [D_1, \ldots, D_n]^T$. The initial values for the modal amplitudes can then be obtained from

$$\{\eta(0)\} = [C]^{-1}\{D\} \tag{43}$$

Note that $[C]$ is not a diagonal matrix. The static deflection profile due to a tip load that yields a tip deflection of 0.06 m is used for $v(x)$. That is,

$$v(x) = 0.06x^2(3L - x)/(2L^3) \tag{44}$$

Two modes are considered and their responses are plotted in Figs. 6 and 7. These figures correctly capture the continuously

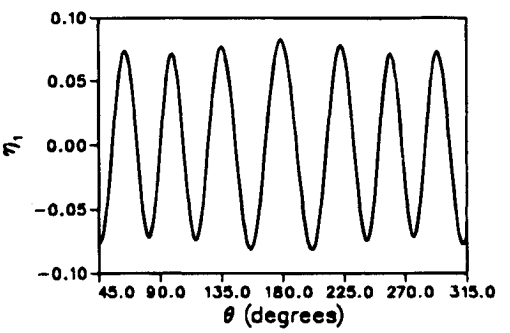

Fig. 6 Time history of η_1 for initial conditions on amplitude.

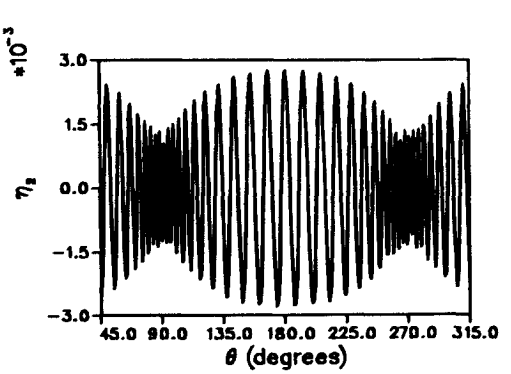

Fig. 7 Time history of η_2 for initial conditions on amplitude.

changing characteristic behavior of the beam. Although both these figures demonstrate an increase and a decrease in the natural frequencies as the end inertia approaches its minimum (zero) and maximum (I_0) values, respectively, it can be observed that the second "mode" is affected much more than the first. As mentioned before, this is not surprising because the boundary condition associated with the end inertia affects the second mode most. The smaller magnitude for the second modal amplitude is due to the fact that the static deflection profile considered is very close to the first mode of the cantilever beam.

The performance of these functions, denoted by ψ_{1r} ($= \phi_r$), $r = 1, \ldots, n_1$, is compared with that of three traditional assumed mode sets next. The modes of a cantilever beam without any end mass or end inertia, denoted by $\psi_{2r}(r = 1, \ldots, n_2)$, correspond to the first traditional mode set. These functions are given in Sec. II. The set ψ_{3r} ($r = 1, \ldots, n_3$) corresponds to the modes of a cantilever beam with an end mass and can be obtained by setting $\theta = 90$ deg in Eqs. (18–24). The number of modes retained is indicated by n_1, n_2, and n_3 for the first, second, and third sets, respectively. The system properties are the same in all three cases. In the second and the third cases, the equations of motion are obtained from the kinetic energy expression given in Eq. (2). The equations of motion are given in Eq. (7). The normalization for ψ_{2r} and ψ_{3r} is as follows:

$$\int_0^L \rho\psi_{2r}(x)\psi_{2s}(x)\,dx = \delta_{rs} \tag{45}$$

$$\int_0^L \rho\psi_{3r}(x)\psi_{3s}(x)\,dx + M_e\psi_{3r}(L)\psi_{3s}(L) = \delta_{rs} \tag{46}$$

The elements of the mass matrix for these cases are given by

$$M^1_{rs} = \delta_{rs} \tag{47}$$

$$M^2_{rs} = \delta_{rs} + M_e\psi_{2r}(L)\psi_{2s}(L) + I_e\psi'_{2r}(L)\psi'_{2s}(L) \tag{48}$$

$$M^3_{rs} = \delta_{rs} + I_e\psi'_{3r}(L)\psi'_{3s}(L) \tag{49}$$

The superscript in the modal mass matrix indicates the trial function set association. The fourth set of trial functions (third traditional set) ψ_{4r} ($r = 1, \ldots, n_4$) correspond to the exact eigenfunction set for the $\theta = \theta(t = 0)$ configuration. That is, these functions satisfy both the natural boundary conditions at $x = L$ at time $t = 0$. However, ψ_{4r} satisfy Eq. (47) for this configuration only, and similar to ψ_{2r} and ψ_{3r} are time invariant. Therefore, the time history of response for the mode set ψ_{4r} is generated using Eq. (7).

The responses are compared for the case of an impulse striking the beam at $x = L$ and $t = 0$. The modal forces are computed from

$$f^k_i = \int_0^L \rho\psi_{ki}(x)\hat{\delta}(x - L)\bar{\delta}(t)\,dx, \quad k = 1, \ldots, 4; \quad i = 1, \ldots, n_k \tag{50}$$

$$= \rho\psi_{ki}(L)\bar{\delta}(t) \tag{51}$$

The impulse is denoted by $\bar{\delta}(t)$ and $\hat{\delta}$ represents the Dirac delta function. The initial values for the modal rates are obtained from the impulse-momentum relationship,

$$[M^k]\,\{\dot{\eta}^k(0)\} = \{f^k\}, \qquad k = 1, \ldots, 4 \tag{52}$$

Once again, the superscript k indicates the trial function set association.

Two modes are considered for the first and fourth sets ($n_1 = n_4 = 2$). The number of modes included for the remaining sets is varied. The complete nonlinear systems of equations are numerically integrated using the fourth-order Runge-Kutta integration method. A unit value for the impulse is considered for the first mode set, and the values for the other sets are computed so that the initial energy in the system is the same for all the models. For all the cases, $\theta(t = 0) = 45$ deg and $\dot{\theta} = 0.5$ rad/s. The tip deflection is plotted in Fig. 8 for all the four cases and for $n_2 = n_3 = 2$.

We observe from Fig. 8 that only the results obtained using the fourth set approximate those from using the exact set well. The performance of the second and third sets is poor. Based on the convergence results for structural systems one would expect the fidelity to improve as the number of modes is increased for the second and third sets. To find if this expectation holds, n_2 and n_3 are increased to four and the tip deflection time history is plotted for the first three mode sets in Fig. 9. We conclude from Fig. 9 that this expectation appears to hold. However, we observe that this expectation clearly does not hold when we examine the response in Fig. 10 corresponding to $n_2 = n_3 = 8$. This is the point to be made. The intuition mentioned in this paragraph is based on a linear analysis adopted from the theory of structural dynamics. Clearly, Eq. (7) does not correspond to the standard structural dynamics equation.

One characteristic that can be observed in Figs. 8–10 is that the amplitude of vibration for the second and third sets reduced as the number of modes is increased. This is because of the energy constraint imposed in obtaining the impulse magnitude for these sets. On the other hand, the response due to an initial deflection profile for the beam cannot be used because computation of the initial values for the amplitudes from Eq. (7) (with all time derivatives set equal to zero) will not yield the values that correspond to the system on hand. The use of ψ_{2r} and ψ_{3r} will yield the values for a cantilever system (no end mass or inertia) and a cantilever with an end mass (no end inertia), thus both will yield erroneous results. This indeed points to the complexity of the system under study.

In all of the cases, we observe that the largest discrepancies occur at times near $t = 1.57$ and 4.71 s. These are precisely the times near which the inertia end condition vanishes ($\theta = 90$ deg and $\theta = 270$ deg, respectively). Note that in the 5-s period of the simulation, the end mass has not even completed half a revolution. Based on these simulation results, we expect the performance of ψ_{2r}, ψ_{3r} and ψ_{4r} to deteriorate if the experiment is conducted over a longer period or if the rotational speed of the end mass is larger.

With regard to the fourth set, we conclude that considering the exact eigenfunctions corresponding to the $t = 0$ configuration yields better results in contrast to the other traditional mode sets considered. However, the performance of ψ_{4r} deteriorates rapidly as the rotational speed of the end mass increases. This can be concluded from Fig. 11 in which the results for the case of $\dot{\theta} = 1.0$ rad/s and the same remaining initial conditions considered in the previous example are shown. The simulation results are plotted for only the first and the fourth trial function sets. The angular rate of 1.0 rad/s is not large at all when one realizes that if the experiment is conducted such that the acceleration due to gravity is along the (positive or negative) z direction in Fig. 1, the pendulum frequency for the end mass is about π rad/s. If the end mass is released from a horizontal position, the maximum angular rate will be about 4.42 rad/s.

VII. Discussion

Significant changes in frequencies occur as the value of the end inertia varies from zero to maximum or vice versa. The nature of the component eigenvalue problem is completely different for these two extreme values of the end inertia. When the end inertia is identically equal to zero, so is the bending moment at that end. When the end inertia is not identically zero, however small its value may be, the bending moment at that end cannot be identically zero so that the rotational inertia force can be balanced by the internal bending moment at that end. This results in a completely different component characteristic behavior for the beam vibration corresponding to zero and nonzero values for the end inertia. Based on the numerical

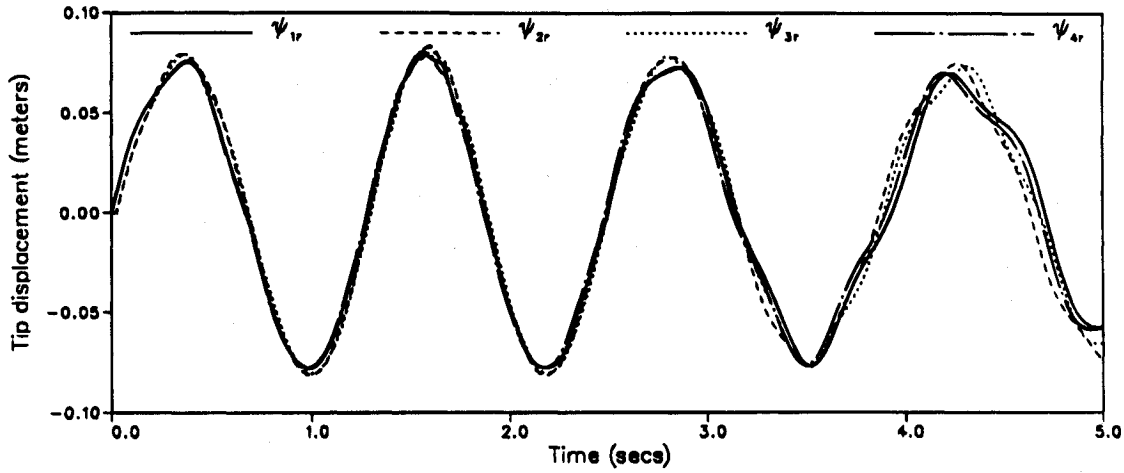

Fig. 8 Impulse response with $n_1 = n_2 = n_3 = n_4 = 2$, $\dot{\theta} = 0.5$ rad/s.

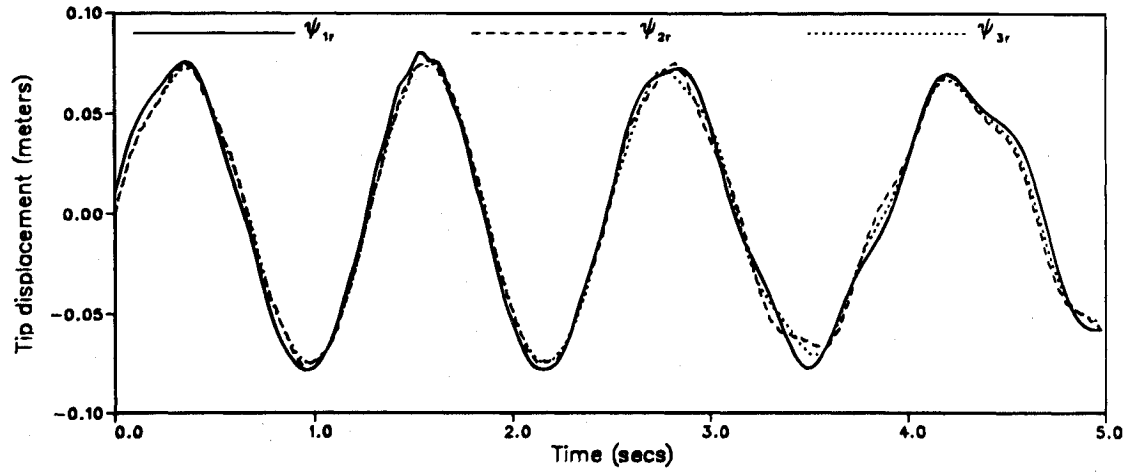

Fig. 9 Impulse response with $n_1 = 2$, and $n_2 = n_3 = 4$, $\dot{\theta} = 0.5$ rad/s.

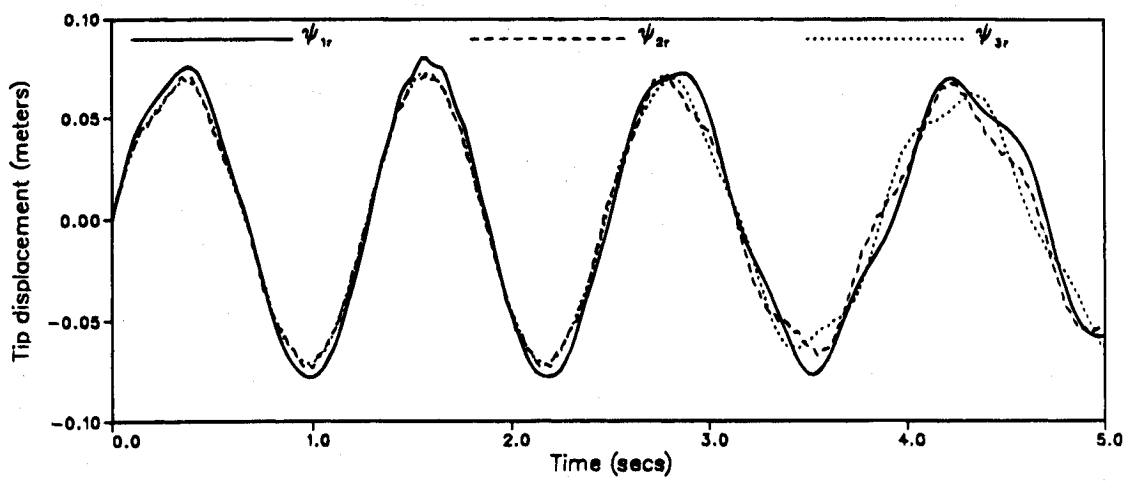

Fig. 10 Impulse response with $n_1 = 2$, and $n_2 = n_3 = 8$, $\dot{\theta} = 0.5$ rad/s.

results presented, we conclude that the critical point is the transition between the no bending moment and the nonzero bending moment end conditions.

For beam-like structures with well-separated natural frequencies, one can easily identify the modes that get affected most due to changes in the outboard body orientations. However, such an identification will not be a trivial task for multibody systems containing flexible structures that require detailed finite element models.

For example, consider the two articulated solar array system shown in Fig. 12. The two panels are connected together by a hinge that permits articulation about the hinge axis. One panel can be reoriented with respect to the other through a rotation about this axis. This panel configuration is similar to the one used in the Gravity Probe B satellite. The way this system is modeled in articulated multibody dynamics codes such as TREETOPS[3] is that first component modes for each of the arrays are obtained separately using finite element analyses.

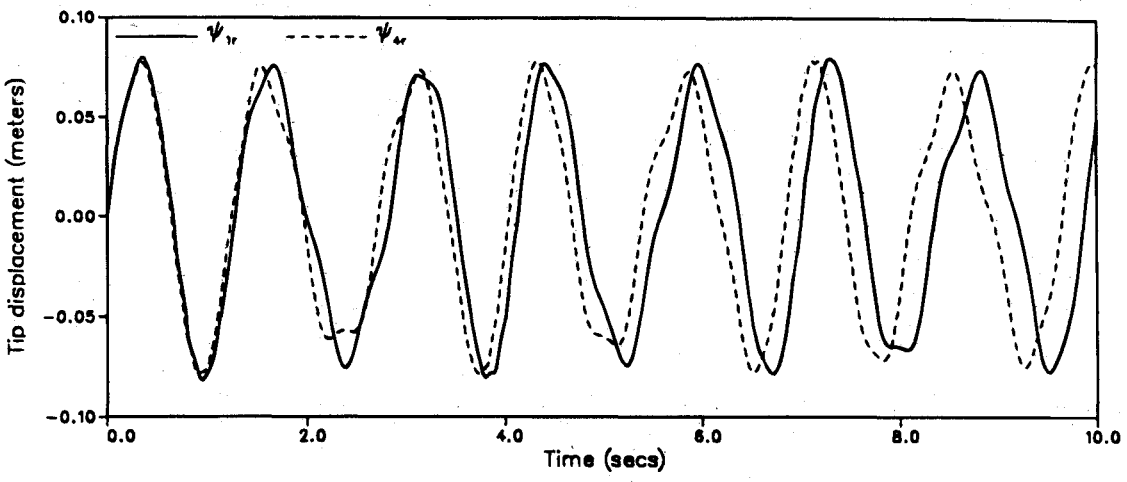

Fig. 11 Comparison with $\dot{\theta} = 1.0$ rad/s, $n_1 = n_2 = 2$.

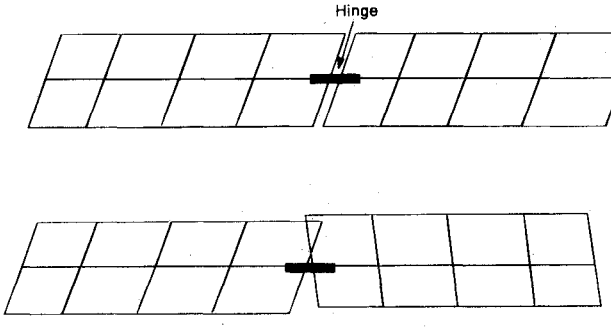

Fig. 12 Solar arrays in two configurations.

Table 2 Natural frequencies of solar panels in two configurations

	Frequency, rad/s	
i	$\theta = 0$ deg	$\theta = 90$ deg
1	5.6236	5.6308
2	9.4366	9.1876
3	29.2586	29.2586
4	31.5919	34.4161
5	40.9209	34.8968
6	89.0767	89.0767
7	103.6575	140.3418
8	153.1356	147.3831
9	176.9963	153.1356
10	220.3361	220.3361

Then, the system dynamic response is obtained using the multibody dynamics code. The "system" natural frequencies can be obtained from a linearized model of the complete system.

Let $\theta = 0$ deg and $\theta = 90$ deg describe the two configurations in Fig. 12. Assuming that the hinge across these panels is locked, the natural frequencies of this system for these two configurations, obtained from a one body model in NASTRAN with free-free end conditions, are shown in Table 2. It can be seen that the characteristics of the system in these two configurations are markedly different. This is significant from a control perspective. The migration of the frequencies may result in controller instabilities. This is precisely the characteristic the user must be aware of when modeling the component body flexibility for both simulating the dynamics of and designing a controller for multibody systems. Although "system modes" are used here to illustrate this point, component modes can also be used to arrive at the same conclusion.

Designing a controller for such a system is also not trivial. This is because such systems are not only time varying, but also nonlinear. Based on the results presented, we conclude that if a linearized model corresponding to the minimum (zero) inertia end condition is used for such purposes, that model will not be valid even within a 1-deg range for the end inertia orientation. This is because, as demonstrated, very small changes in the end inertia orientation cause large changes in system characteristics.

VIII. Conclusions

The effects of outboard body motions on the dynamics of a flexible branch body in a nonplanar multibody system are investigated in this paper. To the authors' knowledge, their importance is addressed here for the first time. Whereas component modes in planar articulated multibody systems are affected by the outboard body masses, nonplanar configurations increase the level of complexity by an order of magnitude because the inertias of the outboard bodies are often time varying. This results in a continuous change in the component body characteristics such as frequencies during the articulation of outboard bodies. The effects of such changes are demonstrated in this paper using a flexible cantilever beam with an articulated payload at its tip. The payload rotates in a plane perpendicular to the beam axis. The boundary condition associated with the moment balance at the payload end changes as the payload articulates.

A set of shape functions that account for such a change are derived for this system in this paper. These functions yield a modal mass block in the dynamics equations that is diagonal and time invariant. This is an attractive feature for analyzing systems containing heavy outboard bodies. Numerical simulation results indicate that these shape functions are better suited to model the dynamics of the system than three "traditional" assumed mode sets. Increasing the number of component modes in two of these three traditional sets did not result in convergence. Only the set that is the solution to the eigenvalue problem associated with the initial configuration and a nonzero end inertia value yielded comparable results for low articulating speeds. However, their performance deteriorated at higher speeds. Application to other problems is discussed. Issues related to control and payload repositioning (involving acceleration and deceleration) will be investigated in the future.

References

[1] Baruh, H., and Tadikonda, S. S. K., "Issues in the Dynamics and Control of Flexible Robot Manipulators," *Journal of Guidance, Control, and Dynamics*, Vol. 12, No. 5, 1989, pp. 659–671.

[2] Book, W. J., "Recursive Lagrangian Dynamics of Flexible Manipulator Arms Via Transformation Matrices," *International Journal of Robotic Research*, Vol. 3 No. 3, 1984, pp. 87–101.

[3] Singh, R. P., Vander Voort, R. J., and Likins, P. W., "Dynamics of Flexible Bodies in Tree Topology—A Computer-Oriented Approach," *Journal of Guidance, Control, and Dynamics*, Vol. 8, No. 5, 1985, pp. 584–590.

[4] Cannon, R. H., Jr., and Schmitz, E., "Initial Experiments on the End-Point Control of a Flexible One-Link Robot," *International Journal of Robotics Research*, Vol. 3 No. 3, 1984, pp. 62–75.

[5] Juang, J. N., Horta, L., and Robertshaw, H. H., "A Slewing Control Experiment for Flexible Structures," *Journal of Guidance, Control, and Dynamics*, Vol. 9, No. 5, 1986, pp. 599–607.

[6] Korolov, V. V., and Chen, Y. H., "Controller Design Robust to Frequency Variation in a One-Link Flexible Robot Arm," *Journal of Dynamic Systems, Measurement and Control*, Vol. 111, March 1989, pp. 9–14.

[7] Menq, C.-H., and Xia, J. Z., "Experiments on the Tracking Control of a Flexible One-Link Manipulator," *Journal of Dynamic Systems, Measurement and Control*, Vol. 1, No. 15, June 1993, pp. 306–308.

[8] Meirovitch, L., *Computational Methods in Structural Dynamics*, Sijthoff-Noordhof, Alphen aan den Rijn, The Netherlands, 1980.

[9] Tadikonda, S. S. K., and Baruh, H., "Gibbs Phenomenon in Structural Mechanics," *AIAA Journal*, Vol. 29, No. 9, 1991, pp. 1488–1497.

[10] Hecht, N. K., and Junkins, J. L., "Near-Minimum-Time Control of a Flexible Manipulator," *Journal of Guidance, Control, and Dynamics*, Vol. 15, No. 2, 1992, pp. 477–481.

[11] Oakley, C. M., and Cannon, R. H., Jr., "Theory and Experiments in Selecting Mode Shapes for Two-Link Flexible Manipulators," *Proceedings of the First International Symposium on Experimental Robotics* (Montreal, Canada), 1989.